Retardation effects on quantum reflection from an evanescent-wave atomic mirror

R. Côté and B. Segev*
Institute for Theoretical Atomic and Molecular Physics (ITAMP), Harvard-Smithsonian Center for Astrophysics, 60 Garden Street, Cambridge, Massachusetts 02138

M. G. Raizen
Department of Physics, The University of Texas at Austin, Austin, Texas 78712-1081
(Received 19 May 1998)

We calculate the reflection probability for ultracold sodium atoms incident on an evanescent-wave atomic mirror. For low enough energies the reflection probability curves exhibit quantum effects that are sensitive to the long-range part of the potential and can therefore be used to resolve Casimir retardation effects. We also explore the accuracy of model potentials approximating the exact atom-wall effective potential.
[S1050-2947(98)08811-8]

PACS number(s): 42.50.Vk, 34.20.−b

I. INTRODUCTION

An electromagnetic mirror for neutral atoms was first suggested by Cook and Hill in 1982 [1]. Their idea was to use the radiation force of an evanescent-electromagnetic wave outside a dielectric surface to repel slow atoms. Such an evanescent wave is formed when light undergoes total internal reflection at the dielectric-vacuum interface. The induced dipole force is repulsive if the light is tuned toward higher frequencies than the corresponding natural dipole frequency of the atom, and attractive if tuned toward lower frequencies. This *evanescent-wave atomic mirror* was realized experimentally by Balykin *et al.* [2]. Almost perfect reflection was demonstrated by using laser light of high intensity to create the evanescent wave, and Na atoms incident on the mirror in grazing angles so as to minimize their velocity at the direction perpendicular to the dielectric surface. Normal incidence reflection in the form of an atomic ''trampoline,'' where atoms falling onto the mirror surface due to gravity bounce back up because of the evanescent wave, has also been demonstrated [3,4].

Recent work in atom optics has emphasized, on the one hand, the need to develop elements, like mirrors and lenses, for the coherent manipulation of atomic matter waves [5]. On the other hand, the experimental progress brought about the ability to cool and launch atoms with extremely low and well-defined velocities [6]. This, combined with the ability to continuously vary the effective potential of the mirror by changing the intensity and the frequency of the laser light, motivates both theoretical and experimental studies of fundamental and practical aspects of the evanescent-wave mirror.

Experimental applications of the evanescent-wave mirror already include a variety of studies. It was recently incorporated into an atomic interferometer [7]. The presence of the reflected atoms near the dielectric-vacuum interface changes the index of refraction outside the dielectric prism and with it, the phase of the reflected laser beam. This phase shift can be used to detect the passage of a cloud of atoms without destroying the coherence of the reflection [8]. Experiments with a time-dependent mirror, in which the potential changes rapidly and continuously by controlled modulation of the intensity of the laser light, were performed [9]. The use of evanescent-light mirrors to build a surface trap was recently reported [10], and the creation of an atomic funnel was also proposed [11]. The penetration depth and wave vector of the evanescent-electromagnetic waves were studied using on resonance laser atomic spectroscopy [12]. Finally, atom guiding using evanescent waves in small hollow optical fibers was demonstrated [13].

In the simplest theoretical approach, the center-of-mass motion of the atom is treated classically while the atom-mirror interaction is derived from a model of a two-level system in the electromagnetic field of the evanescent laser light. Neglecting spontaneous emission, internal transitions, and the attractive van der Waals interaction between the atom and the dielectric surface, the interaction of the atom and the mirror is then described by an exponentially decaying optical potential. Although one would like to preserve as simple a physical picture of the reflection as possible, for actual experiments it may be important to give a more complete treatment.

We consider here the following questions. Is the center of mass motion of the atom properly described by classical mechanics or does it exhibit quantum effects? Is the reflection sensitive to the atom-dielectric attractive interaction, and how sensitive is it to details of the potential curves? Can it be used to distinguish among different theoretical models, for example, resolving retardation effects?

Aspect and collaborators studied an analytical solution of the Schrödinger equation obtained by neglecting the attractive atom-wall interaction, and identified both classical and pure-quantum regimes [14]. The same group later used the reflection from an evanescent-wave atomic mirror in the classical regime to measure the van der Waals force between the dielectric surface and the atom in its ground state, demonstrating that the attractive interaction can hardly be neglected [15], as was also demonstrated by Desbiolles *et al.* [16]. The purpose of this paper is to give a quantum treat-

*Present adderess: Department of Chemistry, Ben-Gurion University, Beer Sheva 84105, Israel.

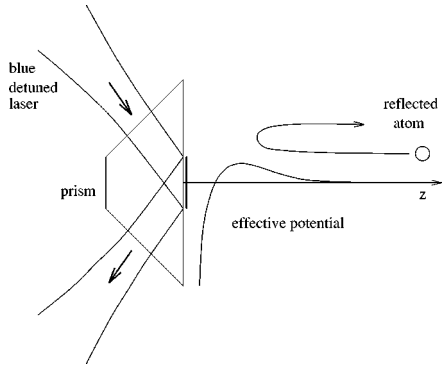

FIG. 1. Schematic of an atomic mirror. The blue-detuned laser light produces a repulsive force, after total internal reflection. An approaching atom will feel the effective potential formed by the atom-wall and light induced potentials and be reflected. Classically, the atom is reflected only if its incoming energy E is less than the barrier height $V_{\max}$, contrary to the quantum regime where it can be reflected even if $E > V_{\max}$.

ment of the reflection, which takes the attractive interaction into account.

In a recent Rapid Communication, we have shown that the center-of-mass motion of cold atoms incident on the evanescent-wave atomic mirror with sufficiently small velocities (e.g., 10.0 cm/s for sodium atoms) will exhibit quantum dynamics [17]. We predicted an S-shaped probability curve, which is typical of quantum behavior, for the fraction of reflected atoms as a function of the logarithm of the laser intensity, and suggested a way to measure it by minimizing the variation of the intensity across the atomic mirror. We have also referred to the possibility of observing Casimir retardation effects in the reflection process. However, at that time we were not able to make definite predictions as to the magnitude of the retardation effects because an exact potential curve including the QED effects for a ground-state sodium atom and the dielectric prism was not yet calculated.

In this paper we review the previous results in more detail and present new ones. In particular, the numerical method that we have used for the calculations is presented and reflection from the physical potential is compared to the reflection from model potentials. Finally, we use recently calculated potential curves [18] to obtain precise predictions for the size and nature of the QED retardation effects on the quantum reflection probability curves.

The experimental setting considered here and depicted in Fig. 1 relates to an uniform flux of Na atoms with an average velocity of a few cm/s and a velocity dispersion of a few mm/s that would be created and launched in the direction normal to a dielectric prism. The repulsive optical potential of an evanescent wave of blue-detuned laser light would combine with the attractive atom-wall interaction to create an effective potential barrier for the atoms. The flux of reflected atoms would be measured.

Such an atomic beam with subrecoil velocity spread conditions has been demonstrated experimentally by the group of Phillips [19]. In this work, a Bose condensate of 10^6 sodium atoms was formed. The momentum spread was reduced to 0.1 recoil (3 mm/s) by adiabatic expansion of the condensate. The atoms were then used in an atomic interferometer. This method can be combined with accelerating optical lattices to launch a subrecoil sample with negligible heating, as described by Raizen, Salomon, and Niu [6]. Atom-surface scattering experiments can be performed by launching the atoms in an upward (nearly vertical) parabolic trajectory, with the surface in the vertical direction.

We show that the long-range (Casimir) interactions due to retardation have in this case an observable effect on the quantum reflection probabilities and that the classically forbidden above-barrier reflection is particularly sensitive to details of the atom-surface potential. If measured, this would constitute a low-energy experimental signature of QED effects, and would supplement recent different measurements of the Casimir forces, e.g., in cavity QED [20].

The theoretical analysis is divided into two steps. First, in Sec. II, we discuss the effective potential, and second, in Sec. III, we analyze the time evolution of the particle in this potential. There are standard physical assumptions and approximations involved in being able to treat the process in this way. Note the apparent contradiction between the two steps. The internal structure of the atom is essential for the evaluation of the potential curves in the first step. In general, an effective potential for an atom or a molecule is the result of changes to its internal structure. Optical potentials, for example, are determined by the space dependence of the atom's energy levels, and therefore of the induced dipole interaction with the laser's electric field. In the second step, however, after a potential curve has been determined, one solves for the dynamics, i.e., for the time evolution of the particle in the given potential, treating the atom as a pointlike structureless particle. The disregard of the internal structure of the atom, at the second step of the calculation is justified by the assumption that actual changes to this internal structure can be neglected, while the space dependence of the effective potentials is the result of virtual, not actual, transitions. For optical potentials, for example, this amounts to neglecting spontaneous emission. This approximation renders our treatment meaningful only in the large detuning regime. Further discussion of this point can be found, for example, in [21]. In Sec. IV, we give the results of our calculations for the reflection probability curves with and without retardation. Finally, discussion and conclusions are presented in Sec. V.

II. ATOMIC MIRROR: THE POTENTIAL CURVE

A. Optical potential

Optical potentials are one example where an effective potential for cold atoms is induced by space-dependent changes to the internal energy of the atoms. In the same way as electric fields induce Stark shifts and magnetic fields induce Zeeman shifts, radiation fields have been shown to induce light shifts to the atom's level structure, thereby creating controlled and adjustable effective potentials. These potentials are important in the field of atom optics as they enable the coherent manipulation of atoms.

A simple successful model for the interaction of a two-level atom with the radiation of a single-mode laser and the vacuum fluctuations was given within the dressed atom approach to light-induced potentials [21]. By solving the optical Bloch equations in the electric dipole approximation, one finds that two forces act on the atom in its ground state: a radiation pressure force and a dipole force [21]. The dipole

TABLE I. Parameters used in this paper. The values of C_3^{metal} and K_4^{metal} are taken from Karchenko *et al.* [25], and $K_4^{(n)}$ is from [17]. We also give the sodium atom mass in atomic units.

Parameter	Value
ϵ	3.258
n	1.805
k_L	5.645×10^{-4} a.u.
θ	45°
κ	4.4771×10^{-4} a.u.
C_3^{metal}	1.889 a.u.
$C_3^{(n)}$	1.0017342 a.u.
K_4^{metal}	2676.71 a.u.
$K_4^{(n)}$	1081.03 a.u.
m	41907.782 a.u.

force can be described by the effective potential

$$V_{\text{dipole}}=\frac{\hbar\delta}{2}\ln\left[1+\frac{\Omega^2/2}{\delta^2+\Gamma^2/4}\right], \tag{1}$$

where Ω is the Rabi frequency, and $\delta\equiv\omega_L-\vec{k}_L\cdot\vec{p}-\omega_0$ is the detuning from the atomic resonance of frequency ω_0 and natural linewidth Γ of an atom of momentum $\vec{p}$ interacting with photons of momentum $\vec{k}_L$ and frequency ω_L. For large detuning the dipole force dominates [21] and the potential reduces to

$$V_{\text{dipole}} \overset{\text{large }\delta}{\rightarrow} \frac{\hbar\Omega^2}{4\delta}, \tag{2}$$

with $\Omega^2\propto Id^2$ where I is the laser intensity and d is the atomic dipole. The dipole potential is therefore proportional to the intensity of the laser and inversely proportional to detuning. The dipole force can be attractive or repulsive, according to the sign of the detuning. For red detuning $\omega_L<\omega_0$, $\delta<0$, and the atom is attracted by high intensity, in accordance with the classical intuition for a dipole in a field. However, for blue detuning, $\omega_L>\omega_0$, $\delta>0$, and the atom is repelled by high intensity. This repulsion is being used in the evanescent-wave atomic mirror.

B. Atom-dielectric interaction with and without retardation effects

The simplest model for the interaction of a ground-state atom and a wall of dielectric constant ϵ considers the interaction between a dipole $\vec{d}$ and its mirror image and gives the Lennard-Jones potential,

$$V_{\text{LJ}}=-\left(\frac{\epsilon-1}{\epsilon+1}\right)\left(\frac{\langle d_{\|}^2\rangle+2\langle d_{\perp}^2\rangle}{64\pi\epsilon_0}\right)z^{-3}=-\frac{C_3^{(n)}}{z^3}, \tag{3}$$

where $\langle d_{\|}^2\rangle$ and $\langle d_{\perp}^2\rangle$ are the expectation values of the squared dipole parallel and perpendicular to the surface [22], $\epsilon=n^2$ and n is the index of refraction of the dielectric. This expression for the potential is approximately valid for constant ϵ and small z. $C_3^{(n)}$ is related to the constant C_3 of a pure metallic wall by $C_3^{(n)}=C_3(n^2-1)/(n^2+1)$. The numerical values for Na atoms used in this paper are given in Table I.

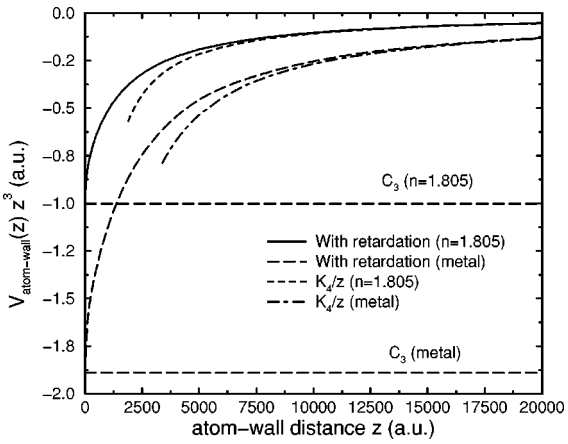

FIG. 2. Atom-wall potential $V_{\text{atom wall}}$ for a conducting and a dielectric wall (with $n=1.805$). Also shown are the asymptotic forms K_4/z^4 and the Lennard-Jones forms C_3/z^3. We plot $V(z)z^3$ as a function of z so that C_3/z^3 becomes a straight line. Numerical values of C_3 and K_4 are given in Table I. For both metallic and dielectric walls, retardation effects reduce the strength of the potential, and the potentials take their asymptotic form near $z\sim5000a_0$.

If we take into account retardation effects, the Casimir-Polder potential is obtained where the finite propagation time between the dipole and its image results in a different asymptotic power-law behavior [23],

$$\lim_{z\rightarrow\infty} V_{CP}(z)\propto z^{-4}. \tag{4}$$

The complete QED treatment gives

$$V_{\text{QED}}(z)=-\frac{\alpha^3}{2\pi}\int_0^\infty d\xi\xi^3\mathbf{d}(i\xi)\int_1^\infty dp e^{-2\xi zp\alpha}\zeta(p,\epsilon), \tag{5}$$

where

$$\zeta(p,\epsilon)\equiv\frac{\sqrt{\epsilon-1+p^2}-p}{\sqrt{\epsilon-1+p^2}+p}+(1-2p^2)\frac{\sqrt{\epsilon-1+p^2}-\epsilon p}{\sqrt{\epsilon-1+p^2}+\epsilon p}, \tag{6}$$

and $\mathbf{d}(i\xi)$ is the dynamic dipole polarizability function [24].

Using semiempirical results for the dynamic dipole polarizability, the numerical integration of Eq. (5) was performed to obtain accurate QED potential curves [25]. We present in Fig. 2 the result of a recent calculation [18] of $V_{\text{QED}}(z)$ for sodium and a dielectric prism with the index of refraction considered here, namely, $n=1.805$ [26]. The deviation from the Lennard-Jones potential of Eq. (3) as well as the Casimir-Polder asymptotic behavior of Eq. (4) are clearly demonstrated.

C. Effective potential of the evanescent-wave mirror

An evanescent-wave mirror for cold atoms is created when a blue-detuned laser beam ($\delta>0$) with wave number $\vec{k}_L$ undergoes total internal reflection inside a dielectric prism. The optical dipole potential V_{optical} for the atom is proportional to the intensity of the laser beam, which drops

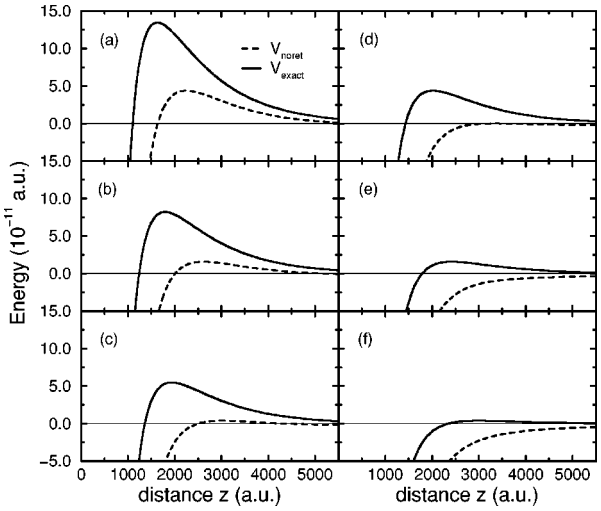

FIG. 3. The effective potential with retardation V_{exact} (solid line) and without retardation $V_{\text{no ret}}$ (dashed line) as a function of the distance z for various values of the laser intensity and hence of C_0. The parameters of these potentials are given in Tables I and II. As the value of C_0 decreases from (a) to (f), the barrier diminishes and is pushed out. Notice that, for (e) and (f), there is no barrier for the case without retardation $V_{\text{no ret}}$.

exponentially with the distance z outside the surface of the dielectric prism. The optical potential is therefore

$$V_{\text{optical}} = C_0 \exp(-2\kappa z)\exp(-\rho^2), \tag{7}$$

with

$$\kappa = k_L \sqrt{n^2 \sin^2\theta - 1}, \tag{8}$$

where $C_0 \propto Id^2/\delta$, the refractive index of the prism is n, and the incident angle is θ. The $\exp(-\rho^2)$ factor accounts for the Gaussian profile of the focused laser beam. We have shown in Ref. [17] that this Gaussian profile is of considerable importance for analyzing experimental results due to the averaging over a cloud of incoming atoms and that minimizing this averaging effect is essential for observing quantum behavior. In the following, we assume a constant intensity and set $\rho^2 = 0$ for simplicity.

The exponentially decaying optical potential and the attractive atom-wall interaction add up to generate an effective potential barrier. It is given by one of the following two formulas, which, respectively, neglect retardation effects or take them into account,

$$V_{\text{no ret}}(z) = C_0 \exp(-2\kappa z) - \frac{C_3^{(n)}}{z^3}, \tag{9}$$

$$V_{\text{exact}}(z) = C_0 \exp(-2\kappa z) + V_{\text{QED}}(z), \tag{10}$$

where V_{QED} is depicted in Fig. 2. The various numerical values used here are listed in Table I. The height of the barrier $V_{\max}$ vary as a function of the intensity of the laser beam, as do its location and shape. This is illustrated in Fig. 3. One can see that as the intensity is reduced, the barrier is decreasing in height and is moving out to larger distances. For a barrier with $V_{\max} = \frac{1}{2} m v_{\text{top}}^2$ corresponding to sodium atoms with $v_{\text{top}} = 10.0$ cm/s, the top of the barrier is located at a distance of roughly $2000 a_0$, i.e., far out from the prism itself. This enables us to treat the system without taking into account many surface phenomena, e.g., the sticking of the atoms to the surface, the creation of phonons, etc.

TABLE II. Parameters for the potential curves of Fig. 3. For a given value of the optical potential intensity C_0, there are two potential curves, V_{exact} with retardation and $V_{\text{no ret}}$ without retardation. For each graph we give the height of the potential $V_{\max}$ as well as the corresponding velocity v_{top}, ($V_{\max} = \frac{1}{2} m v_{\text{top}}^2$), the location of the maximum of the barrier $z_{\max}$, and the curvature α at the top of the barrier. For $V_{\text{no ret}}$ of Figs. 3(e) and 3(f), there is no barrier, hence no $V_{\max}$, v_{top}, $z_{\max}$, and α.

Figure	C_0 (10^{-10} a.u.)	Type	$V_{\max}$ (10^{-11} a.u.)	v_{top} (cm/s)	$z_{\max}$ (units of a_0)	α (10^{-16} a.u.)
3(a)	9.877	ret.	13.454	17.53	1629.5	−3.7754
		no ret.	4.378	10.00	2243.4	−1.0531
3(b)	7.463	ret.	8.207	13.69	1793.0	−2.1277
		no ret.	1.576	6.00	2614.9	−0.4077
3(c)	6.023	ret.	5.483	11.19	1935.2	−1.3649
		no ret.	0.394	3.00	3022.2	−0.1542
3(d)	5.375	ret.	4.378	10.00	2017.5	−1.0541
		no ret.	0.013	0.54	3334.6	−0.0739
3(e)	3.391	ret.	1.576	6.00	2416.9	−0.3447
		no ret.				
3(f)	2.119	ret.	0.394	3.00	3000.4	−0.0828
		no ret.				

Since one is probing distances in the neighborhood of $2000 a_0$ and more, one could expect to be in a regime where retardation effects could be noticeable. Indeed, when the distance between the atom and the wall becomes of the order of the transition wavelength $\lambda/2\pi$, the time of flight of the virtual photons becomes large enough to cause retardation effects. For sodium, $\lambda/2\pi = 1772 a_0$, and a barrier located at $2000 a_0$ should probe retardation corrections. In fact, one notices from Fig. 2 that retardation corrections for the dielectric considered in this paper become important near that distance. To illustrate this, we also plotted the effective potentials with and without retardation corrections in Fig. 3: the height, its location and the curvature of the potential at the top of the barrier vary strongly when one compares the two sets of effective potentials. For small enough values of C_0, the barrier disappear [see $V_{\text{no ret}}$ in Figs. 3(e) and 3(f)], but quantum reflection still occurs, as we discuss below. The numerical parameters corresponding to V_{exact} and $V_{\text{no ret}}$ of Fig. 3 are given in Table II.

III. REFLECTION FROM POTENTIAL BARRIERS

A. Numerical calculation of the reflection probability

In this section, we elaborate on the specific numerical computations involved in the evaluation of the reflection probability for an arbitrary potential. As described in Côté *et al.* [27], our procedure is based on matching a superposi-

tion of incoming and reflected Wentzel-Kramers-Brillouin (WKB) waves to an exact or accurate approximate solution of the Schrödinger equation bridging the region where the WKB approximation is inaccurate.

The potential curves of Eqs. (9) and (10) and Figs. 2 and 3 are defined only for $z>0$. In a complete treatment the potential should be properly modified at $z=0$ to account for the presence of the interface with the dielectric layer. We assume perfect sticking at the dielectric surface and neglect any reflection from the region closer to the interface than some finite small z, determined numerically as explained below. Under this assumption, the singularity at $z=0$ is of no physical importance and we solve for the reflection from the potential barriers of Eqs. (9) and (10) in the same way we would have solved for the reflection from a bounded finite range potential.

We apply a numerical calculation in which we propagate a wave function and an auxiliary function, defined in Eq. (20) below, from $z\rightarrow+\infty$ inward. Assuming perfect sticking at the surface, we prove that this auxiliary function converges to the reflection probability as $z=0$ is approached. In the proof, we assume that the potential that vanishes for $z\rightarrow+\infty$, takes a constant negative value $-V_0$ for $z\rightarrow-\infty$. We then show that the value of V_0 does not influence Eq. (20), which is all we need for the calculation itself.

In order to obtain Eq. (20) which converges to the reflection probabilities of a particle of mass m and kinetic energy $E=\hbar^2k^2/2m$, incident on the barrier from the right, we formally consider the reciprocal problem of the particles incident from $z\rightarrow-\infty$ with kinetic energy $\hbar^2k'^2/2m$ where k' is defined by $E+V_0=k'^2\hbar^2/2m$. According to the reciprocity relation, the reflection probability is the same whether the atom is incident on a barrier from the left or the right. (A proof is given in Appendix A for the configuration of a step function.)

Coming from $z\rightarrow-\infty$, the exact wave function can be approximated by the WKB ansatz,

$$\psi_{\mathrm{WKB}}(E,z)=\frac{1}{\sqrt{p(E,z)}}\left[\exp\left(\frac{i}{\hbar}\int_{z_m}^{z}p(E,z')dz'\right)+R_{\mathrm{WKB}}\exp\left(-\frac{i}{\hbar}\int_{z_m}^{z}p(E,z')dz'\right)\right], \tag{11}$$

where z_m is an arbitrary matching point, and we are assuming that in the entire region $z\leqslant z_m$, the essential condition for applicability of the WKB approximation is valid. Namely, that the de Broglie wavelength $\lambda=2\pi\hbar/p$, with

$$p(E,z)=\sqrt{2m[E-V(z)]}, \tag{12}$$

varies sufficiently slowly,

$$\delta\lambda\equiv\frac{1}{2\pi}\left|\frac{d\lambda}{dz}\right|=\hbar\left|\frac{m}{p^3}\frac{dV}{dz}\right|\ll 1. \tag{13}$$

In the remainder of the paper, we refer to the regions where the condition (13) is not fulfilled as ''badlands.'' In Fig. 4, we illustrate these ''badlands'' for the exact potentials shown in Fig. 3: a more complete discussion is given in the next section.

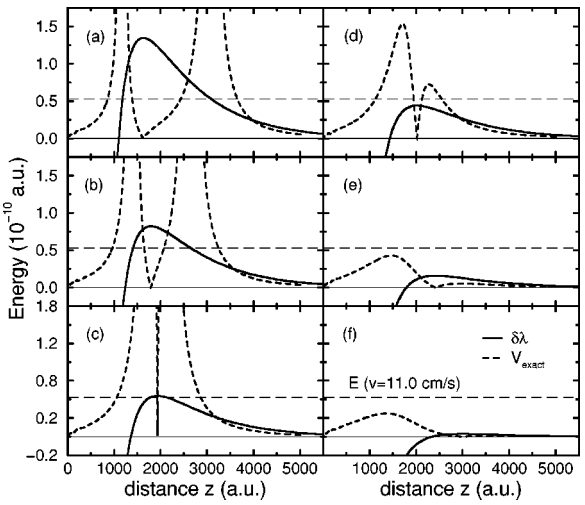

FIG. 4. The dimensionless badlands $\delta\lambda$ (dashed lines) for the exact potentials V_{exact} of Fig. 3 (solid line), for an incoming atom with $E=5.2975\times10^{-11}$ a.u. (or $v=11.0$ cm/s). The potential V_{exact} and energy E (the horizontal dashed line) are on a scale of 10^{-10} a.u., and the badlands on a unit scale. (a), (b), and (c) correspond to tunneling through the barrier (the classical turning points are indicated by the intersection of E with V_{exact}) and (d), (e), and (f) represent the above-barrier cases. [The legend shown in (f) applies for all plots.]

By requiring Eq. (11) to asymptotically ($z\rightarrow-\infty$) match the exact wave function $\exp(ik'z)+R\exp(-ik'z)$ we find

$$R_{\mathrm{WKB}}=R\exp[i\eta(z_m)], \tag{14}$$

i.e., that R_{WKB} and the conventionally defined reflection amplitude R differ by a phase $\eta(z_m)$ that accounts for the fact that the matching point z_m is not at $z=0$, and that the local momentum p may differ from its asymptotic value $\hbar k'$ at finite values of z:

$$\eta(z_m)=2\lim_{z\rightarrow-\infty}\left(\frac{1}{\hbar}\int_{z_m}^{z}p(E,z')dz'-k'z\right). \tag{15}$$

Knowing a wave function $\psi(z)$ (exact or accurate approximation) corresponding to a purely outgoing wave at $z\rightarrow+\infty$, we can determine the reflection amplitude by matching at z_m the logarithmic derivatives of the WKB wave function and $\psi(z)$ [Eq. (11)],

$$R_{\mathrm{WKB}}=-\frac{\psi'(z_m)/\psi(z_m)-\frac{i}{\hbar}p(z_m)+\frac{p'(z_m)}{2p(z_m)}}{\psi'(z_m)/\psi(z_m)+\frac{i}{\hbar}p(z_m)+\frac{p'(z_m)}{2p(z_m)}}. \tag{16}$$

The usual reflection amplitude R can be obtained from R_{WKB} through the phase correction (14), and the reflection probability is simply

$$\mathcal{R}=|R|^2=|R_{\mathrm{WKB}}|^2. \tag{17}$$

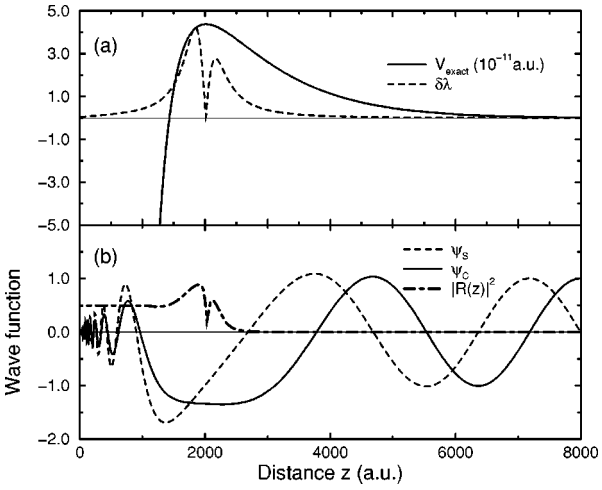

FIG. 5. In (a), we show V_{exact} corresponding to Fig. 3(d) (with $v_{\text{top}}=10.0$ cm/s) and the badlands $\delta\lambda$ for a sodium atom incident on the prism with a velocity $v=10.1$ cm/s. The real (ψ_C) and imaginary (ψ_S) parts of the wave function (in arb. units) are plotted in (b), as well as the dimensionless auxiliary function $\mathcal{R}(E,z)=|R(z)|^2$ as it approaches the reflection probability $\mathcal{R}(E)=|R|^2$ at small z. Convergence is reached after the wave functions have passed through the badlands.

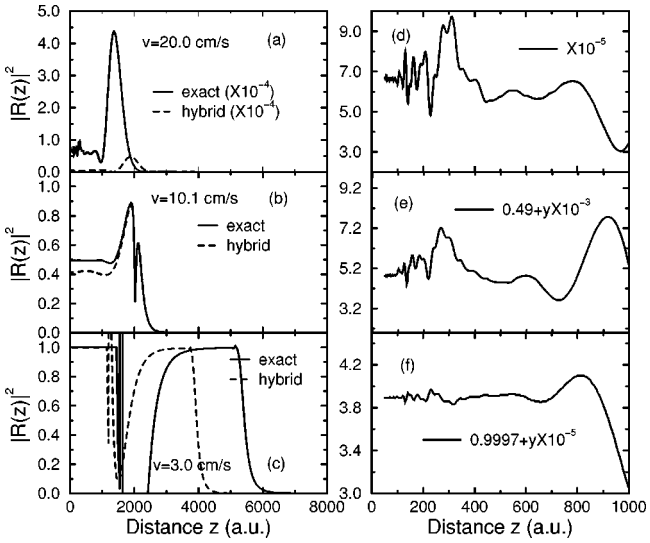

FIG. 6. The dimensionless auxiliary function $\mathcal{R}(E,z)=|R(z)|^2$ as it approaches the reflection probability $\mathcal{R}(E)=|R|^2$ at small z, for three incoming velocities: 20.0 cm/s in (a), 10.1 cm/s in (b), and 3.0 cm/s in (c), for the exact potential V_{exact} of Fig. 3(d) (solid line) and the hybrid potential V_{hyb} of Fig. 8(c) below (dahsed line). Both potentials have a height corresponding to $v_{\text{top}}=10.0$ cm/s. (d), (e), and (f) show enlargements of the convergence region (at small z) for V_{exact}: in (d), $|R(z)|^2$ oscillates between 3×10^{-5} and 9×10^{-5}, in (e) between 0.4932 and 0.4992, and in (f) between 0.999 730 and 0.999 742. Finally, the values of $\mathcal{R}(E)$ for the exact and hybrid potentials, are: in (a) 6.91×10^{-5} and 3.99×10^{-6}, in (b) 0.4948 and 0.4192, and in (c) 0.999 738 9 and 0.997 813 4, respectively.

Equation (16) is used to derive the results and predictions presented below from an accurate numerical solution of the stationary Schrödinger equation obtained by propagating two independent solutions from large z inward toward $z=0$: $\psi_C(z)$ and $\psi_S(z)$. They are, respectively, defined by the boundary conditions at $z\to\infty$,

$$\psi_C(z)\to\cos(kz), \tag{18}$$

$$\psi_S(z)\to\sin(kz). \tag{19}$$

An auxiliary reflection probability function is then defined by

$$\mathcal{R}(E,z)=\left|\frac{\partial_z\ln\psi(z)+\frac{1}{2}\partial_z\ln p(z)-\frac{i}{\hbar}p(z)}{\partial_z\ln\psi(z)+\frac{1}{2}\partial_z\ln p(z)+\frac{i}{\hbar}p(z)}\right|^2, \tag{20}$$

where

$$\psi(z)\equiv\psi_C(z)+i\psi_S(z). \tag{21}$$

Note that Eq. (20) does not depend on V_0 or k', and that the singularity at $z\to0$ is avoided. The auxiliary function $\mathcal{R}(E,z)$ approaches the actual reflection probability as z approaches zero,

$$\mathcal{R}(E)=\lim_{z\to0}\mathcal{R}(E,z). \tag{22}$$

In Fig. 5, for example, we present the solution $\mathcal{R}(E,z)$ for an incoming sodium atom with velocity $v=10.1$ cm/s incident on a potential barrier V_{exact} (calculated with retardation), of height $V_{\max}=\frac{1}{2}mv_{\text{top}}^2$ with $v_{\text{top}}=10.0$ cm/s, and the corresponding ''badlands.'' As the atom approaches the barrier from $+\infty$, it reaches the border of the outer badland (where $\delta\lambda$ is not negligible) located around $3000a_0$: the wave functions ψ_C and ψ_S start to be affected and $\mathcal{R}(E,z)$ begins to grow from its initial zero value [see Fig. 5(b)]. Its behavior follows the shape of the badlands. One notices that although the wave functions oscillate rapidly because of the singularity at the origin, $\mathcal{R}(E,z)$ is well behaved right after the badlands are passed. In Figs. 6(a)–6(c), we also present the numerical calculation of $\mathcal{R}(E,z)$ for energies high above and way below the same barrier and the corresponding badlands are plotted in Figs. 7(a)–7(c). (These figures contain also results for an hybrid potential discussed in a next section.) The behavior of $\mathcal{R}(E,z)$ as it converges to $\mathcal{R}(E)$ is general: we obtain the same pattern for all three cases. Going inward, $\mathcal{R}(E,z)$ grows first at the approach of the outer badland [if it is sizable as in (b) and (c) but not (a)] and overshoots its asymptotic value before decreasing until the inner badland starts. It then grows again and reaches another maximum before correcting its value by decreasing too much, to finally stabilize its value to $\mathcal{R}(E)$. In Figs. 6(d)–6(f), we demonstrate the convergence more explicitly by enlarging the region near $z=0$: in all three cases, the behavior is similar and convergence is reached at $z\sim100a_0$.

B. Quantum versus classical reflection

A classical particle with mass m and velocity v (momentum $\hbar k=mv$) incident on a one-dimensional potential barrier $V(z)$ can be either transmitted or reflected. The classical reflection probability is a Heavyside function $\mathcal{R}_{\text{classic}}(E)$

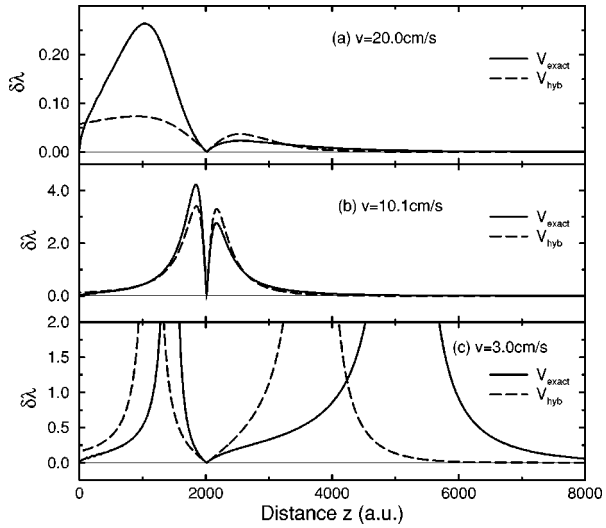

FIG. 7. Comparison of the dimensionless badlands $\delta\lambda$ between the exact (solid line) and the hybrid (dashed line) potentials shown in Fig. 8(c), for different incoming velocities (or energies): (a) 20.0 cm/s (much higher than $V_{\max}$ corresponding to $v_{\text{top}}=10.0$ cm/s), (b) 10.1 cm/s (just above v_{top}), and (c) 3.0 cm/s (much lower than v_{top}).

$\equiv\Theta(V_{\max}-E)$, where $E=\frac{1}{2}mv^2$ is the energy of the atom and $V_{\max}=\max[V(z)]$ is the height of the potential barrier. In quantum mechanics the reflection probability $\mathcal{R}(E)$ is a smooth function of the energy: the classical step function is replaced by a quantum S-shaped curve, with a finite overbarrier reflection probability as well as a finite underbarrier transmission (or tunneling) probability.

Traditionally, one compares the de Broglie wavelength of the particle, $\lambda_{dB}=2\pi\hbar/mv$, with some scale in the potential, say, the width of the potential barrier, to determine if substantial quantum behavior should be expected. According to our analysis, while the underbarrier transmission is mostly sensitive to the width and height of the barrier, the overbarrier reflection is determined by regions of the potential where the semiclassical treatment fails. The concept of the ''badlands'' was introduced to quantify these regions [27]. In Fig. 4, we illustrate $\delta\lambda$ for a sodium atom with $v=11.0$ cm/s going through the exact atom-wall potential, i.e., with retardation corrections. Figs. 4(a)–4(c) show the case of tunneling, and as one can expect, the regions where the system cannot be described by WKB are located near the classical turning points, i.e., when $V(z)=E$ or alternatively $p(z)=0$. As the height of the barrier is progressively decreased (by lowering the intensity of the laser), the turning points are getting closer to each other: the total region spent by badlands is diminished, hence a larger tunneling probability. Notice that the inner badland is steeper than the outer one because the slope of the potential is larger near that turning point; for the same reason, the outer badland is more extended. When the barrier is lowered further as in Figs. 4(d)–4(f), there are no turning points anymore, but the badlands persist with the same ''topography,'' namely, a steeper inner badland and a more extended outer one. From Figs. 6(d)–6(f), one notices that $\mathcal{R}(E,z)$ takes on its value after passing through the regions where the condition (13) is not satisfied. For above barrier reflection [see Figs. 6(a) and 6(b) or Figs. 4(d)–4(f)], we observe a larger effect of the inner badland than the outer one, and conclude that most of the above-barrier reflection is caused by the inner portion of the effective potential, contrary to normal intuition.

For underbarrier energies the badlands are centered around the turning point, their height extending to infinity. For above barrier energies there are no turning points, but two badlands can still be recognized. In this respect the concept of the badlands includes the concept of turning points but is more general. Note that close enough to the dielectric-vacuum interface there is no badland and WKB applies, which is the reason why $\mathcal{R}(E,z)$ converges to $\mathcal{R}(E)$.

C. Model potentials

While numerical calculation is the only way to obtain accurate predictions for a realistic effective potential, it is often helpful to consider simplified models that can be solved exactly. In this section three models are presented for the potential barrier of the evanescent wave mirror, and closed form formulas for the probabilities are obtained from the analytic solutions to the corresponding equations. After studying different model potentials, we found that a better agreement with the exact results was obtained when the barrier's height and curvature were chosen to fit the exact physical potential. Keeping these parameters fixed, we chose three potentials with very different asymptotic behaviors:

$$V_{\cosh}(z)=V_{\max}\cosh^{-2}[(z-z_{\max})/\zeta], \tag{23}$$

$$V_{\text{osc}}(z)=V_{\max}\{1-[(z-z_{\max})/\zeta]^2\}, \tag{24}$$

$$V_{\text{hyb}}(z)=\begin{cases} V_{\cosh}(z), & z>z_{\max} \\ V_{\text{osc}}(z), & z<z_{\max}. \end{cases} \tag{25}$$

All these potentials have the same height $V_{\max}$ and curvature α at the top of the barrier as the exact physical potential,

$$\alpha\equiv\partial^2V/\partial z^2|_{z=z_{\max}}=-2V_{\max}\zeta^{-2}. \tag{26}$$

Both parameters $V_{\max}$ and α depend on C_0, i.e., on the intensity of the laser, and are sensitive to retardation effects, as depicted in Fig. 3 and given in Table II. Solving for V_{osc} gives the leading order in a semiclassical approximation, as it amounts to replacing the potential by the closest inverted harmonic oscillator [28].

As proven in Appendix B, the reflection probabilities from these potentials are, respectively, given by

$$\mathcal{R}_{\cosh}(E)=\frac{\cos^2(\pi u)}{\cos^2(\pi u)+\sinh^2(\pi k\zeta)}, \tag{27}$$

$$\mathcal{R}_{\text{osc}}(E)=\frac{1}{1+\exp(-2\pi a)}, \tag{28}$$

$$\mathcal{R}_{\text{hyb}}(E)=\left|\frac{l(1-F)-i(1+F)}{l(1-F)+i(1+F)}\right|^2, \tag{29}$$

where

$$l=\sqrt{1+\exp(2\pi a)}-\exp(\pi a), \tag{30}$$

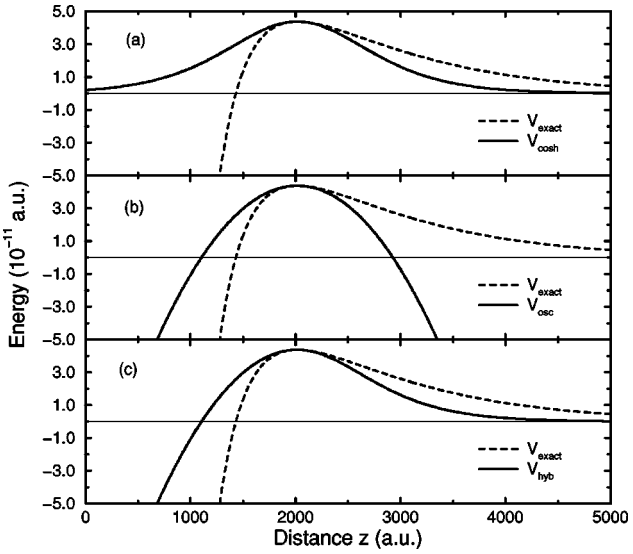

FIG. 8. The three model potentials: (a) $V_{\cosh}$, (b) $V_{\rm osc}$, and (c) $V_{\rm hyb}$. Each of them is matched to $V_{\rm exact}$ with $V_{\max}=4.378\times10^{-11}$ a.u. (or $v_{\rm top}=10.0$ cm/s) located at $z_{\max}=2017.53$ a.u. with a curvature of $\alpha=-1.054\,08\times10^{-16}$ a.u. (see also Table II).

$$F=(\zeta v_0)^{-1/2}\times\frac{\left|\Gamma\left(\frac{1}{4}+\frac{ia}{2}\right)\right|}{\left|\Gamma\left(\frac{3}{4}+\frac{ia}{2}\right)\right|}\frac{\Gamma\left(\frac{3}{4}+\frac{u}{2}-\frac{i\zeta k}{2}\right)\Gamma\left(\frac{3}{4}-\frac{u}{2}-\frac{i\zeta k}{2}\right)}{\Gamma\left(\frac{1}{4}+\frac{u}{2}-\frac{i\zeta k}{2}\right)\Gamma\left(\frac{1}{4}-\frac{u}{2}-\frac{i\zeta k}{2}\right)} \tag{31}$$

with the notation

$$k\equiv\sqrt{2mE}/\hbar, \tag{32}$$

$$v_0\equiv\sqrt{2mV_{\max}}/\hbar, \tag{33}$$

$$u\equiv\sqrt{1/4-(v_0\zeta)^2}, \tag{34}$$

$$a\equiv\sqrt{\frac{m}{-\alpha}}(V_{\max}-E). \tag{35}$$

The model potentials are shown in Figs. 8(a)–8(c) for a barrier height $V_{\max}=4.378\times10^{-11}$ a.u. (corresponding to a sodium atom with velocity $v_{\rm top}=10.0$ cm/s), with $\alpha=-1.05408\times10^{-16}$ a.u. From Fig. 8, one expects $V_{\rm hyb}$ to be the best approximation to the exact potential $V_{\rm exact}$. In order to analyze the results from $V_{\rm exact}$ and $V_{\rm hyb}$, we compare in Figs. 7(a)–7(c) their badlands for three different velocities of the incoming sodium atoms: 20.0 cm/s, 10.1 cm/s, and 3.0 cm/s. Since $V_{\rm hyb}$ is a combination of the two symmetric potentials $V_{\cosh}$ and $V_{\rm osc}$, their badlands are given by the symmetric image of the $V_{\rm hyb}$ badlands about $z=z_{\max}$. The auxiliary functions $\mathcal{R}(E,z)$ for $V_{\rm exact}$ and $V_{\rm hyb}$ at the same three velocities are shown in Figs. 6(a)–6(c), as they converge to the reflection probabilities. $\mathcal{R}(E)$ for the exact and hybrid potentials, was found to be: in (a), $\mathcal{R}=6.91\times10^{-5}$ and 3.99×10^{-6}, in (b) $\mathcal{R}=0.4948$ and 0.4192, and in (c) $\mathcal{R}=0.999\,738\,9$ and $0.997\,813\,4$, respectively. In the first, and last, example with $v=20.0$ cm/s, and $v=3.0$ cm/s, the energy of the atom is much higher, or much lower, than the barrier height, respectively. In both cases, the badlands of the model and exact potentials are extremely different, and so are the probabilities. In the second example ($v=10.1$ cm/s), where $E\sim V_{\max}$ near the top of the barrier, the agreement between the badlands is better, and a fairly good agreement for $\mathcal{R}(E)$ is obtained.

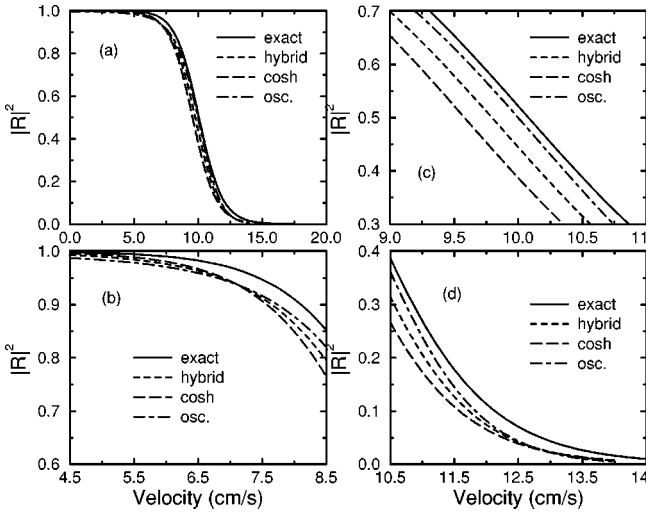

FIG. 9. Comparison of the three models and the exact reflection probability $\mathcal{R}(E)=|R|^2$ for sodium atoms incident on a barrier of height $V_{\max}=\frac{1}{2}mv_{\rm top}^2$ with $v_{\rm top}=10.0$ cm/s. (a) shows the curves as a function of v, and (b), (c), and (d) enlarge the low-, medium-, and high-velocity regimes, respectively. Overall, $V_{\rm hyb}$ is a better approximation to $V_{\rm exact}$, $V_{\rm osc}$ being the best for $v\sim v_{\rm top}$ and $V_{\cosh}$ at velocities far from $v_{\rm top}$.

We computed $\mathcal{R}(E)$ for the exact and three model potentials of Fig. 8 as a function of the velocity of the incoming atom. We illustrate the results in Figs. 9(a)–9(d): in (a), we observe that the four curves are very close to each other, implying that the model potentials adjusted to the parameters of $V_{\rm exact}$ give good results. In (b)–(d), we enlarge three different portions of the same graph, corresponding to small velocities where tunneling is present, velocities for which the atom energy is near the top of the barrier ($v_{\rm top}=10.0$ cm/s), and larger velocities where above-barrier reflection is dominant. The hybrid potential gives an overall better agreement to the exact curve than the two other model potentials. At smaller v [see (b)], $V_{\cosh}$ is the best model and $V_{\rm osc}$ the worst up to $v\sim6.75$ cm/s, at which point the three models are equivalent. In the range of velocities near the top of the barrier [in (c)], we have the reverse, namely that $V_{\rm osc}$ is the closest to the exact curve and $V_{\cosh}$ the farthest. This remains true up to $v\sim12.75$ cm/s, at which point the $V_{\cosh}$ is once again the best model and $V_{\rm osc}$ the worst one [see (d)]. For all values of v, the model potentials give curves below the exact one, and the $V_{\rm hyb}$ is always between $V_{\cosh}$ and $V_{\rm osc}$. This can be understood by looking at the potentials themselves (see Fig. 8) or at the badlands (see Fig. 7).

Overall, if one is interested at the reflection probability for a given potential barrier, one can get good approximate results by using one of the three models depending on which energy regime is considered. The first step to such an approximation is to fit the two parameters, namely, the height of the barrier and the curvature at its top, for each case considered.

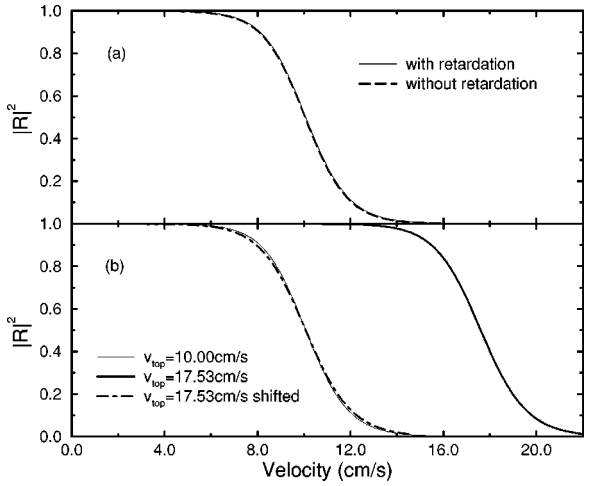

FIG. 10. Comparison of the reflection probability $\mathcal{R}(E)=|R|^2$ for the exact V_{exact} and Lennard-Jones $V_{\text{no ret}}$ potentials as a function of the incident velocity v. In (a), both have the same height $V_{\max}$ (or $v_{\text{top}}=10.0$ cm/s), and in (b), both have the same C_0 (or laser intensity) which produces different barrier heights ($v_{\text{top}}=17.53$ cm/s for V_{exact} and 10.0 cm/s for $V_{\text{no ret}}$). In figure (b), we also shifted the exact curves by 7.53 cm/s$=9.877\times10^{-10}$ a.u. to superpose it with the Lennard-Jones curves: although still small, the shape difference is larger than in (a).

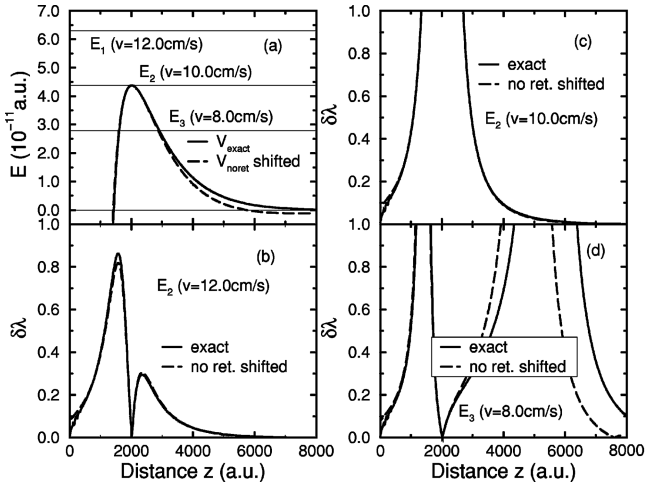

FIG. 11. In (a), we compare V_{exact} (solid line) and $V_{\text{no ret}}$ (dashed line) for values of C_0 corresponding to Fig. 10(a), i.e., a barrier with $v_{\text{top}}=10.0$ cm/s. The potential without retardation is shifted by $225.9a_0$ to the left to overlap with V_{exact} (see Table II). V_{exact} has a longer tail and a faster decrease at smaller distances than $V_{\text{no ret}}$. We also show the energies corresponding to three velocities, namely $v=12.0$, 10.0, and 8.0 cm/s. In (b), (c), and (d), we plot the badlands for the same three velocities: here again, the curves without retardation have been shifted by $225.9a_0$ to explicitly show any difference for the case with retardation.

IV. RESOLVING RETARDATION EFFECTS

We now turn our attention to the detection of retardation effects in above-barrier reflection and quantum tunneling. Retardation affects the reflection probability curves in two different ways: by shifting their reflection threshold and by changing their shape. Using the technique described above, we evaluate the reflection probability $\mathcal{R}(E)$ for sodium atoms approaching a dielectric infinite wall with $n=1.805$ (or $\epsilon=3.258$). There are two distinct ways in which an actual experiment can be performed. One can keep the intensity of the laser constant and change the energy of the incoming atoms, or, alternatively, keep a constant energy and vary the intensity of the laser. We show below that in both cases retardation shifts the threshold for reflection. However, the change in the shape of the curves is mainly observable as one varies the intensity of the laser and scans different regions of the attractive potential.

A. Fixed potential

We compute and compare the reflection probability $\mathcal{R}(E)$ for two effective potentials, V_{exact} (with retardation), and $V_{\text{no ret}}$ with the Lennard-Jones atom-wall interaction (without retardation). We first compare $\mathcal{R}(E)$ for barriers of the same height ($V_{\max}=4.378\times10^{-11}$ a.u. or, equivalently, $v_{\text{top}}=10.0$ cm/s) and two different values of C_0. The potentials are depicted as the dashed line in Fig. 3(a) (without retardation) and solid line in Fig. 3(d) (with retardation). $C_0=9.877\times10^{-10}$ a.u. for the case without retardation and $C_0=5.375\times10^{-10}$ a.u. for the case with retardation (see Table II). The calculated reflection probabilities are given in Fig. 10(a). Both $\mathcal{R}(E)$ curves are basically identical: no significant retardation effects can be detected. The curve with retardation lies slightly above the curve without retardation since the potential with retardation is less attractive: the long-range form of V_{exact} has a more extended tail than $V_{\text{no ret}}$. We illustrate these observations in Fig. 11(a), where $V_{\text{no ret}}$ has been shifted by $z_{\max}^{\text{no ret}}-z_{\max}^{\text{exact}}$ to overlap with V_{exact}. Indeed, one observes that $V_{\text{no ret}}$ (dashed line) is slightly larger than V_{exact} (solid line) at smaller distances, and vice versa at larger distances. On the same graph, we show three different kinetic energies corresponding to velocities of 12.0 cm/s (above barrier), 10.0 cm/s (or v_{top}), and 8.0 cm/s (below barrier). The corresponding badlands are plotted in Figs. 11(b), 11(c), and 11(d), respectively. As in (a), the curves for $V_{\text{no ret}}$ have been shifted by $z_{\max}^{\text{no ret}}-z_{\max}^{\text{exact}}$ in order to better visualize the differences in $\delta\lambda$. In Fig. 11(b), we notice that $\delta\lambda$ reaches slightly higher values for V_{exact}, hence the slightly larger $\mathcal{R}(E)$ [see Fig. 10(a)]. Similarly, for $v<v_{\text{top}}$, the total range spent with $\delta\lambda\sim1$ is more extended for V_{exact} than for $V_{\text{no ret}}$ [see Fig. 11(c)], leading to less tunneling or more reflection, as noted in Fig. 10(a).

In the second situation illustrated in Fig. 10(b) we consider a case where the intensity of the laser is fixed, the two curves have $C_0=9.877\times10^{-10}$ a.u. corresponding to the potentials of Fig. 3(a). We notice that the threshold is different for the two curves, reflecting the difference in the height of the barriers (corresponding to $v_{\text{top}}=17.53$ cm/s and 10.0 cm/s for V_{exact} and $V_{\text{no ret}}$, respectively). We shifted the curve with retardation by 7.53 cm/s to overlap with the curve without retardation, in order to detect any effect in the shape of $\mathcal{R}(E)$. Once again, the difference is small: the curve for V_{exact} is slightly less steep than for $V_{\text{no ret}}$. By shifting the curve $\mathcal{R}(E)$ for V_{exact}, we actually compare two $\mathcal{R}(E)$ curves with different energy scales, because of the nonlinear relationship between v and E. This amplifies the differences observed in the shapes of $\mathcal{R}(E)$.

From the two situations illustrated in Fig. 10, one concludes that by varying the velocity of the incoming atoms,

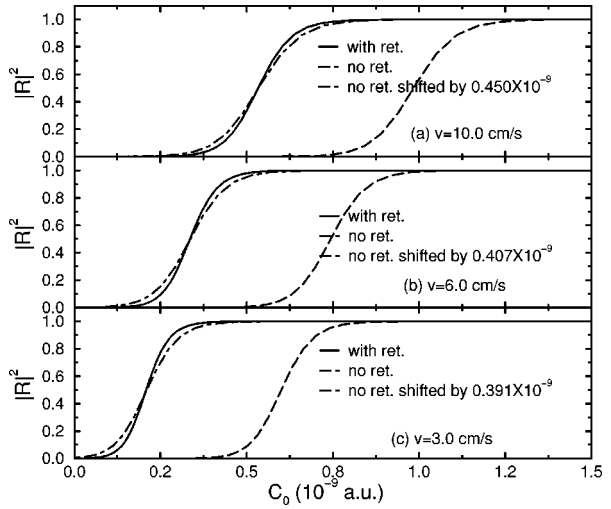

FIG. 12. Comparison of the reflection probability $\mathcal{R}(E)=|R|^2$ as a function of C_0 for the exact (with retardation) and Lennard-Jones (no retardation) potentials, for three different incident velocities: 10.0 cm/s in (a), 6.0 cm/s in (b), and 3.0 cm/s in (c). Near the classical threshold $C_0=C^*$, $(V_{\max}=E)$, the reflection probability increases from zero to one. These thresholds are shifted by the retardation effects. The shifts are larger for higher velocities. They are 4.502×10^{-10} a.u. in (a), 4.072×10^{-10} a.u. in (b), and 3.904×10^{-10} a.u. in (c). The S shape of the curve results from quantum effects and is also sensitive to retardation. As v is decreased, this S shape becomes steeper. To illustrate the variation in shape, with and without retardation, we shift the curves without retardation by the differences in C^*.

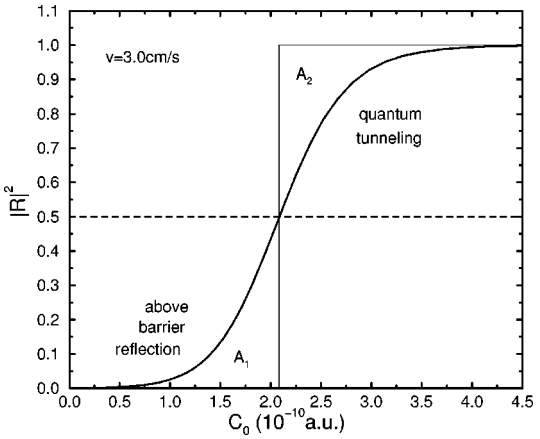

FIG. 13. A reflection probability curve of $\mathcal{R}(E)=|R|^2$ as a function of the laser intensity C_0. The areas A_1 and A_2 correspond to above barrier reflection and quantum tunneling, respectively, and they are defined by the vertical line cutting the curve at $|R|^2=0.5$ located (by definition) at $C_0=C_{1/2}$.

only a threshold change could be measured, the difference in the shape of $\mathcal{R}(E)$ being extremely small.

B. Scanning the attractive potential by varying the laser intensity

A simpler and better experimental setup is to have a source of slow atoms incident on the prism with a given velocity, and to change the shape and extent of the barrier by varying the intensity of the laser, or, similarly, the value of C_0. As C_0 is decreased, the barrier is lowered and moved out. By doing so, one probes different regions of the atom-wall potential and at different rates.

We chose incoming atoms at three different velocities relevant to future experiments: 10.0 cm/s, 6.0 cm/s, and 3.0 cm/s. For each velocity, we computed the reflection probability curves as a function of C_0 for the potentials with and without retardation effects. The results are shown in Fig. 12. For a given energy E (or velocity v), as one changes C_0, one reaches a value $C_0=C^*$ which is the threshold for classical reflection, for which $V_{\max}=E$. We observe a shift in the threshold C^*: for the curve with retardation, it is located at smaller values of C_0 than for the curve without retardation. We shifted $\mathcal{R}(E)$ without retardation by the difference in C^* to illustrate the difference in shape between the two curves. As one can see from Figs. 12(a)–12(c), as we reduce E (or v), the location of the curves with retardation is slightly moved to lower values of C_0, but the curves without retardation are more affected. Moreover, the shift between the two sets of curves for a given value of v decreases slightly as we lower the velocity. This can be understood from examining the potentials in Fig. 3 and the corresponding numbers in Table II. For each case, the location of the top of the barrier at $C_0=C^*$ is moving out as the v is decreased. The barriers at the two threshold cases of Fig. 12(a) are depicted as the dashed curve of Fig. 3(a) (no retardation) and the solid curve of Fig. 3(d) (with retardation), for which $z_{\max}=2243.4a_0$ and $2017.5a_0$, respectively, and the change in $C_0=C^*$ is 4.502×10^{-10} a.u. (see Table II). Similarly, Fig. 11(b) corresponds to the dashed curve of Fig. 3(b) (no retardation) and the solid curve of Fig. 3(e) (with retardation) with $z_{\max}=2614.9a_0$ and $2416.9a_0$, respectively, and $\Delta C^*=4.072\times10^{-10}$ a.u.; and Fig. 11(c) corresponds to the dashed curve of Fig. 3(c) (no retardation) and the solid curve of Fig. 3(f) (with retardation) with $z_{\max}=3022.2a_0$ and $3000.4a_0$, respectively, and $\Delta C^*=3.904\times10^{-10}$ a.u. So, as v is reduced, $z_{\max}$ is moved out, but since the retardation effects reduce the strength of the attractive atom-wall potential with respect to the Lennard-Jones case, the evanescent potential has more relative strength and therefore a smaller C^* is required to get the same barrier height. The farther out $z_{\max}$ is, the weaker $V_{\text{atom wall}}$, and the smaller the difference between the thresholds C^* with and without retardation.

It is visible from Fig. 12 that the shape of the reflection probability curves for potentials with and without retardation differs. To quantify this quantum effect, we define, as shown in Fig. 13, two regions of area A_1 and A_2 delimited by the vertical line at $C_0\equiv C_{1/2}$ intersecting the curve at $\mathcal{R}=0.5$. This almost corresponds to the value of $C_0=C^*$ giving a barrier of height corresponding to the atom velocity (here 3.0 cm/s). In fact, in Fig. 13, $\ln C_{1/2}=-22.291$ a.u. which is very close to $\ln C^*=-22.275$ a.u. (see Table III). We define A_1 and A_2 in respect to $C_{1/2}$ because the exact determination of C^* would be experimentally more difficult. Notice here that classically, the reflection probability curve would be a step function located at C^*, which is well approximated by $C_{1/2}$: the curve for $C_0<C_{1/2}$ represents the effect of above-barrier quantum reflection, and the curve for $C_0>C_{1/2}$ the effect of quantum tunneling. Equivalently, A_1 is a signature of above barrier quantum reflection and A_2 a signature of tunneling.

TABLE III. Quantum reflection and tunneling signatures. $C_{1/2}$ is the value of C_0 that gives $\mathcal{R}=0.5$ while C^* is the value of C_0 for which $V_{max}=E$ (or $v_{top}=v$). A_1 and A_2 (in units of 10^{-11} a.u.) are defined in Fig. 13 and represent above-barrier reflection and quantum tunneling, respectively, for the curves of Fig. 12. Similarly, B_1 and B_2 denote above-barrier reflection and quantum tunneling, respectively, for the curves of Fig. 16. A_1+A_2 and B_1+B_2 are measures of the total quantum signature. For all quantities, we give the ratio ret./no ret. As the velocity v is reduced, the effect of retardation is more pronounced.

Quantity	Type	$v=10.0$ cm/s	$v=6.0$ cm/s	$v=3.0$ cm/s
$\ln C_{1/2}$	ret.	−21.352	−21.815	−22.291
	no ret.	−20.739	−21.019	−21.232
$\ln C^*$	ret.	−21.344	−21.805	−22.275
	no ret.	−20.736	−21.016	−21.230
A_1	ret.	3.2350	2.6049	2.1485
(10^{-11} a.u.)	no ret.	4.0013	3.4540	2.9779
	ratio	0.8085	0.7542	0.7215
A_2	ret.	3.5009	2.8654	2.4245
(10^{-11} a.u.)	no ret.	4.2543	3.6976	3.2683
	ratio	0.8229	0.7749	0.7418
A_1+A_2	ret.	6.7359	5.4703	4.5729
(10^{-11} a.u.)	no ret.	8.2556	7.1516	6.2462
	ratio	0.8159	0.7649	0.7321
B_1	ret.	0.067 96	0.090 89	0.1289
(a.u.)	no ret.	0.043 77	0.050 64	0.054 19
	ratio	1.553	1.795	2.379
B_2	ret.	0.059 24	0.075 15	0.098 26
(a.u.)	no ret.	0.040 31	0.045 95	0.049 86
	ratio	1.470	1.635	1.971
B_1+B_2	ret.	0.1272	0.1660	0.2272
(a.u.)	no ret.	0.084 08	0.096 59	0.010 41
	ratio	1.513	1.719	2.183

Looking at the overlapping curves on Fig. 12(c), we find that $\mathcal{R}(E)$ is larger for $V_{\text{no ret}}$ than for V_{exact} when $C_0 < C_{1/2}$, and vice versa when $C_0 > C_{1/2}$. In other words, the curve with retardation is steeper than the curve without, and the difference is increased as v diminishes. In order to understand the reason for the shape difference in $\mathcal{R}(E)$ with and without retardation illustrated in Fig. 12 (beyond the shift in the value of C^*), we plot in Fig. 14 the potential curves for the three values of incoming velocities ($v=10.0$, 6.0, and 3.0 cm/s), and for each velocity, we consider three values of C_0: $C_{1/2}-\Delta$, $C_{1/2}$, and $C_{1/2}+\Delta$ (where $\Delta = 5.0\times10^{-11}$ a.u.). The energies corresponding to the three velocities are also drawn for each graph. The corresponding badlands are shown in Fig. 15. As was already noted in Fig. 11, we observe that V_{exact} is more extended at large distances, and that the variation in $V_{\text{no ret}}$ is more pronounced. As v is reduced, the shift in z_{max} and the difference in both

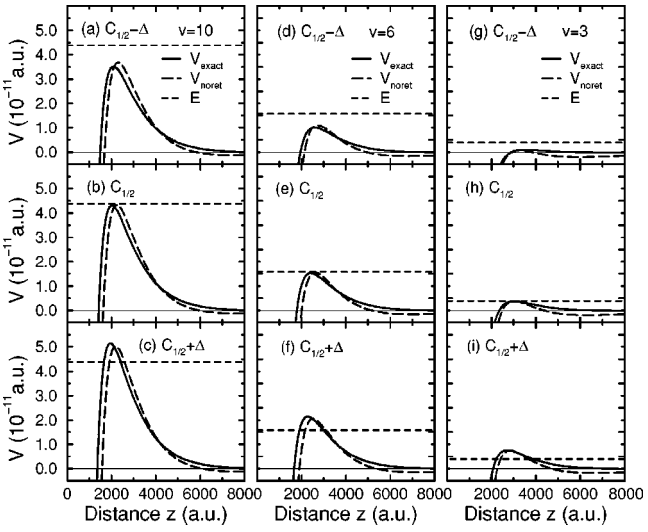

FIG. 14. Potential curves with and without retardation (V_{exact} and $V_{\text{no ret}}$) depicted to explain Fig. 12. In (a), (b), and (c), $E=\frac{1}{2}mv^2$ with $v=10.0$ cm/s, in (d), (e), and (f), $v=6.0$ cm/s, and in (g), (h), and (i), $v=3.0$ cm/s. C_0 (or the laser intensity) was chosen in (b), (e), and (h) to give reflection probability $\mathcal{R}=0.5$ in all these cases, namely, $C_0=C_{1/2}$. For V_{exact} $C_{1/2}$ is 5.333×10^{-10} a.u. in (b), 3.356×10^{-10} a.u. in (e), and 2.085×10^{-10} a.u. in (h); while for $V_{\text{no ret}}$ $C_{1/2}$ is 9.844×10^{-10} a.u. in (b), 7.440×10^{-10} a.u. in (e), and 6.013×10^{-10} a.u. in (h). Equally spaced points in Fig. 12 on both sides of $C_0=C_{1/2}$ for these six cases are depicted in the other graphs, with a spacing of $\Delta=5.0\times10^{-11}$ a.u. V_{exact} is higher than $V_{\text{no ret}}$ for $C_0=C_{1/2}-\Delta$, and vice versa for $C_{1/2}+\Delta$, because $V_{\text{atom wall}}$ is less important for V_{exact}, hence a change in C_0 has a stronger impact. V_{exact} always has a more extended tail.

height and shape between V_{exact} and $V_{\text{no ret}}$ is decreasing as well. This is related to the nonlinear dependence of the effective potentials on C_0: for a higher value of $C_{1/2}$, the optical potential is more dominant, and a change Δ in its value has a stronger effect than for a smaller value of $C_{1/2}$ for

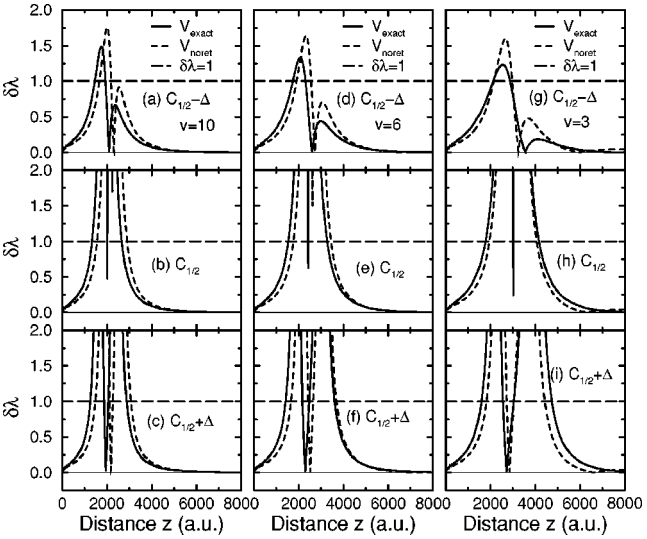

FIG. 15. The badlands $\delta\lambda$ for the potentials of Fig. 14. For above-barrier reflection corresponding to (a), (d), and (g), the badlands for $V_{\text{no ret}}$ are more prononuced than for V_{exact}, hence a larger reflection probability. For quantum tunneling corresponding to (c), (f), and (i), the badlands for V_{exact} are more extended than for $V_{\text{no ret}}$, leading to less tunneling (or a larger reflection probability).

which the nonaffected atom-wall component is relatively more important.

The increasing difference in $\mathcal{R}(E)$ for decreasing velocities despite the fact that the barriers actually look more alike can be understood by examining the badlands of Fig. 15. In Figs. 15(a), 15(b), and 15(c), we show $\delta\lambda$ for three values of C_0 for $v=10.0$ cm/s. For $C_0<C_{1/2}$, in (a), the badlands without retardation (dashed lines) are higher and more extended, hence the smaller above barrier reflection probability for V_{exact}. In (b) $\mathcal{R}(E)=0.5$ by construction, and we do not observe a significant difference in the size of the region spent by $\delta\lambda\sim 1$. For $C_0>C_{1/2}$ shown in (c), we note a more extended $\delta\lambda$ for V_{exact}, hence a larger value for $\mathcal{R}(E)$. As v is decreased, these differences in the badlands become stronger (see Fig. 15), and so do the differences in the probability curves of Fig. 12.

From the above discussion and the curves shown in Fig. 12, it is tempting to conclude that retardation effects reduce the quantum signature in the reflection probability curve. But, as we mentioned before, retardation effects increase slightly $\mathcal{R}(E)$ for constant effective potentials of the same height [see Figs. 10(a) and 11]. Moreover, as was noted in [17] for a conducting wall, retardation effects enhance $\mathcal{R}(E)$. This apparent contradiction can be resolved by realizing that, in fact, we are comparing two very different types of experimental setups. In Fig. 10(a) and [17], the potential is fixed and we compute the reflection probability as a function of the energy or velocity of the incoming atoms. This setup really evaluates the effect of retardation on incoming atoms. On the other hand, the situation explored in Fig. 12 corresponds to a multiple set of experiments: for each value of C_0, the potential is different, and therefore comparing $\mathcal{R}(E)$ for various C_0 is comparing different potentials.

We have computed A_1 and A_2 for the various cases of Fig. 12. They are listed in Table III. As described above, retardation affects the quantum signature more strongly at lower v. The ratio of A_1+A_2 with and without retardation is reduced, indicating a weaker quantum signature with retardation than without. One also notices that above-barrier reflection (ratio of A_1) is slightly more affected than tunneling (ratio of A_2). For $v=3.0$ cm/s, the effect of retardation is of nearly 30%.

In Fig. 16 we plot the same results for $\mathcal{R}(E)$ that were presented in Fig. 12, this time as a function of $\ln C_0$, because it allows the comparison with experiments where averaging over the Gaussian profile of the laser beam is relevant [17]. Because C_0 takes on smaller values, the curves with retardation are more affected than those without: most of the points of the previous discussion seem to be reversed. The shift in threshold $\ln C^*$ is larger as v is decreased, and the curves without retardation (dashed lines) are steeper: the quantum signature appears to be stronger with retardation. Although the logarithmic scale enhances the smaller values of C_0 and hence amplifies the signature of above-barrier reflection more than the quantum tunneling, it is still clear from Fig. 16 that retardation has more influence at lower velocities. As previously, we can quantify the quantum signature by evaluating similar areas as A_1 and A_2, defined this time as an integral over $\ln C_0$: we call them B_1 and B_2, respectively. Their values are also given in Table III. Again, by comparing the ratios of B_1+B_2 as a function of v, we notice that retardation has a stronger effect at lower v. Moreover, from the ratios of B_1 and B_2, we again find that above-barrier reflection is more affected by retardation, although in the reverse order. That difference is also amplified by the logaritmic scale.

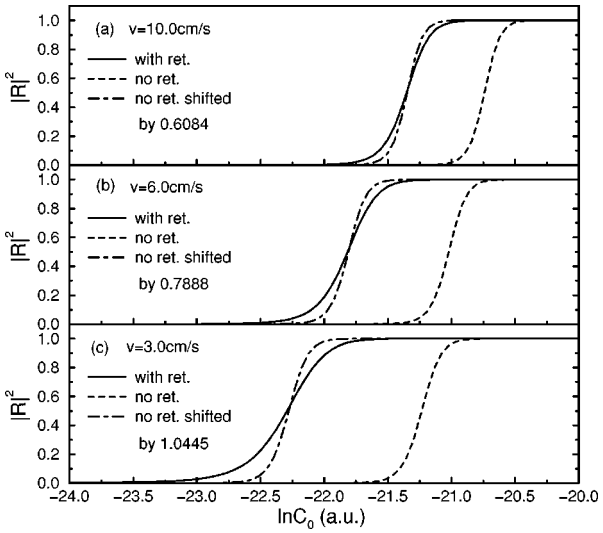

FIG. 16. Same as Fig. 12, but as a function of $\ln C_0$. Because of the logarithmic scaling, the smaller values of C_0 are enhanced, and the curves without retardation are steeper, in contrast to Fig. 12. The quantum signature is amplified, especially the above-barrier reflection that occurs at smaller values of C_0.

V. CONCLUSION AND DISCUSSION

We conclude that retardation effects could be observed in this system and that, in general, quantum effects may be used for very sensitive measurements. Unlike reflection in the classical domain, quantum reflection depends on the details of the potential, both at short and large distances. In the classical regime, i.e., for reflection experiments that could be properly described by classical mechanics, reflection yields can be used to identify thresholds. In the semiclassical regime, the yields are also sensitive to the curvature near the top of the barrier. Quantum reflection probabilities are determined by the complete potential curve. As we have demonstrated, identifying and using parameters in the quantum dynamics regime, i.e., looking for experiments that cannot be described by a semiclassical approximation, is a promising new way to study long-range and short-range atom-surface interactions.

Finally, we would like to comment on some relevant issues that were not considered in our work. While we have used the most accurate available calculations, to our knowledge, for the atom-wall interaction, and have given a complete quantum treatment to the center-of-mass motion of the atoms, we still relied on the following simplifying assumptions, justified by the experimental conditions that we have considered. First, we neglected surface roughness. Studies of surface roughness effects indicate that the mirror allows for specular reflection if the surface is flat at the atomic scale [29]. Note that, for the mirror to be useful for atom-optics applications, it is essential that the reflection process be coherent. Second, we neglected the finite response time of the mirror images in the dielectric, which seems reasonable since

the atoms are moving very slowly. The effect of the response time for the rearrangement of charges in the bulk forming the mirror was studied for metal [30], but to our knowledge, such results are not available for the rearrangement time of the dipole polarizations in dielectrics. Third, we treated the atom as a two-level system, and assumed that no internal transitions take place during the reflection. Observed effects that go beyond the two-level model include state-selective properties of the reflection [2,31], cooling during the reflection through a spontaneous Raman transition between two hyperfine levels [16,32], and, in general, an interplay between internal state transitions and the center-of-mass motion [33]. Further, we did not take into account the dependence of the dielectric constant on frequency, e.g., in the calculations that gave the potential curves for the atom-dielectric interaction using Eq. (5). Finally, looking only at reflection probabilities, we did not study the reflection process in the time domain and we did not look at wave packets. Clearly, some of these issues should be addressed in future research.

ACKNOWLEDGMENTS

The authors are pleased to acknowledge helpful conversations with J. F. Babb and A. Dalgarno. The work of R.C. and B.S. was supported by the National Science Foundation through a grant for the Institute for Theoretical Atomic and Molecular Physics (ITAMP) at the Harvard-Smithsonian Center for Astrophysics. The work of M.G.R. was supported by the National Science Foundation and the R.A. Welch Foundation.

APPENDIX A: RECIPROCITY RELATIONS

In this appendix, we review the reciprocity relations for the reflection and transmission amplitudes. We consider a one-dimensional potential that goes uphill (left to right) from a constant value V_1 at $z\rightarrow-\infty$ to a constant value V_2 at $z\rightarrow+\infty$ (with $V_1<V_2$). For a particle of mass m and kinetic energy E incoming from $-\infty$, one has

$$\underline{z\rightarrow-\infty} \qquad\qquad \underline{z\rightarrow+\infty}$$

$$e^{ik_1 z}+R_{\nearrow}e^{-ik_1 z} \quad\leftrightarrow\quad T_{\nearrow}e^{ik_2 z}, \tag{A1}$$

where $k_1=\sqrt{2m(E-V_1)}/\hbar$ and $k_2=\sqrt{2m(E-V_2)}/\hbar$. $R_{\nearrow}$ and $T_{\nearrow}$ represent the uphill reflection and transmission amplitudes, respectively. The downhill relation going from right to left is

$$T_{\swarrow}e^{-ik_1 x}\leftrightarrow e^{-ik_2 x}+R_{\swarrow}e^{ik_2 x}, \tag{A2}$$

and $R_{\swarrow}$ and $T_{\swarrow}$ now represent the downhill reflection and transmission amplitudes, respectively. Dividing the first relation by $T_{\nearrow}$ and its complex conjugate by $T^*_{\nearrow}$, multiplying the first relation by $R_{\swarrow}$, and adding them together, one gets

$$\left(\frac{R_{\swarrow}R_{\nearrow}}{T_{\nearrow}}+\frac{1}{T^*_{\nearrow}}\right)e^{-ik_1 x}+\left(\frac{R_{\swarrow}}{T_{\nearrow}}+\frac{R^*_{\nearrow}}{T^*_{\nearrow}}\right)e^{ik_1 x} \leftrightarrow e^{-ik_2 x}+R_{\swarrow}e^{ik_2 x}. \tag{A3}$$

By comparing with Eq. (A2), one must have

$$\frac{R_{\swarrow}R_{\nearrow}}{T_{\nearrow}}+\frac{1}{T^*_{\nearrow}}=T_{\swarrow}, \tag{A4}$$

$$\frac{R_{\swarrow}}{T_{\nearrow}}+\frac{R^*_{\nearrow}}{T^*_{\nearrow}}=0. \tag{A5}$$

The second equation implies that $|R|=|R_{\swarrow}|=|R_{\nearrow}|$. Substituting in the first equation, we obtain

$$T_{\swarrow}=\frac{1}{T^*_{\nearrow}}(1-|R|^2), \tag{A6}$$

which, in turn, implies

$$(\text{phase of } T_{\swarrow})=(\text{phase of } T_{\nearrow})=\theta. \tag{A7}$$

Similarly, from the relation between $R_{\swarrow}$ and $R_{\nearrow}$, we find

$$(\text{phase of } R_{\swarrow})=\pi+2\theta+(\text{phase of } R_{\nearrow}). \tag{A8}$$

Finally, from the usual definition of the reflection and transmission probabilities [34], i.e.,

$$\mathcal{R}_{\nearrow}\equiv\frac{v_1}{v_1}\frac{R_{\nearrow}R^*_{\nearrow}}{1}=|R_{\nearrow}|^2, \tag{A9}$$

$$\mathcal{R}_{\swarrow}\equiv\frac{v_2}{v_2}\frac{R_{\swarrow}R^*_{\swarrow}}{1}=|R_{\swarrow}|^2, \tag{A10}$$

$$\mathcal{T}_{\nearrow}\equiv\frac{v_2}{v_1}\frac{T_{\nearrow}T^*_{\nearrow}}{1}=\frac{k_2}{k_1}|T_{\nearrow}|^2, \tag{A11}$$

$$\mathcal{T}_{\swarrow}\equiv\frac{v_1}{v_2}\frac{T_{\swarrow}T^*_{\swarrow}}{1}=\frac{k_1}{k_2}|T_{\swarrow}|^2. \tag{A12}$$

We get

$$\mathcal{R}=\mathcal{R}_{\nearrow}=\mathcal{R}_{\swarrow}=|R|^2, \tag{A13}$$

and since $\mathcal{T}_{\nearrow}=1-\mathcal{R}_{\nearrow}=1-|R|^2$ and $\mathcal{T}_{\swarrow}=1-\mathcal{R}_{\swarrow}=1-|R|^2$,

$$\mathcal{T}=\mathcal{T}_{\nearrow}=\mathcal{T}_{\swarrow} \quad\text{or}\quad \frac{k_2}{k_1}|T_{\nearrow}|^2=\frac{k_1}{k_2}|T_{\swarrow}|^2. \tag{A14}$$

APPENDIX B: REFLECTION PROBABILITIES FOR THE MODEL POTENTIALS

In this appendix we obtain the reflection probabilities for the model potentials of Eqs. (23), (24), and (25), by exactly solving the corresponding stationary Schrödinger equations.

A general solution to the stationary Schrödinger equation with the potential $V_{\cosh}$ is given by [35]

$$\psi_{\cosh}(z)=A\ \cosh^{u+1/2}\left(\frac{z}{\zeta}\right)\times {}_2F_1\left[\frac{1}{4}+\frac{u}{2}+\frac{ik\zeta}{2},\frac{1}{4}+\frac{u}{2}-\frac{ik\zeta}{2},\frac{1}{2};-\sinh^2\left(\frac{z}{\zeta}\right)\right]+B\ \sinh\left(\frac{z}{\zeta}\right)\cosh^{u+1/2}\left(\frac{z}{\zeta}\right)\times {}_2F_1\left[\frac{3}{4}+\frac{u}{2}+\frac{ik\zeta}{2},\frac{3}{4}+\frac{u}{2}-\frac{ik\zeta}{2},\frac{3}{2};-\sinh^2\left(\frac{z}{\zeta}\right)\right], \tag{B1}$$

where A and B are constants, satisfying

$$\psi_{\cosh}(z=0)=A, \tag{B2}$$

$$\left.\frac{\partial\psi_{\cosh}}{\partial z}\right|_{z=0}=B/\zeta. \tag{B3}$$

A general solution to the stationary Schrödinger equation with the potential $V_{\rm osc}$ is given by [36]

$$\psi_{\rm osc}(z)=\nu W(a,z\sqrt{2v_0/\zeta})+\mu W(a,-z\sqrt{2v_0/\zeta}), \tag{B4}$$

where ν and μ are constants, satisfying

$$\psi_{\rm osc}(z=0)=\sqrt{\frac{|\Gamma(1/4+ia/2)|}{|\Gamma(3/4+ia/2)|}}2^{-3/4}(\nu+\mu), \tag{B5}$$

$$\left.\frac{\partial\psi_{\rm osc}}{\partial z}\right|_{z=0}=-\sqrt{2v_0/\zeta}\sqrt{\frac{|\Gamma(3/4+ia/)2|}{|\Gamma(1/4+ia/2)|}}2^{-1/4}(\nu-\mu). \tag{B6}$$

The reflection probability $\mathcal{R}_{\cosh}\equiv|R_{\cosh}|^2$ for the potential $V_{\cosh}$ is obtained by finding a specific solution to the Schrödinger equation, i.e., a choice of $A=A_{\cosh}$ and $B=B_{\cosh}$ for Eq. (B1) that would satisfy

$$\lim_{z\to-\infty}\psi_{\cosh}=\exp(-ikz), \tag{B7}$$

taking the limit $z\to\infty$ and identifying the asymptotic coefficients,

$$\lim_{z\to\infty}\psi_{\cosh}=\frac{1}{T_{\cosh}}\exp(-ikz)+\frac{R_{\cosh}}{T_{\cosh}}\exp(ikz). \tag{B8}$$

The reflection probability $\mathcal{R}_{\rm osc}\equiv|R_{\rm osc}|^2$ for the potential $V_{\rm osc}$ is obtained in a similar way by finding $\nu_{\rm osc}$ and $\mu_{\rm osc}$ that would satisfy

$$\lim_{z\to-\infty}\psi_{\rm osc}=\sqrt{\frac{2}{|z|}}\exp[i\phi(z)], \tag{B9}$$

$$\phi(z)\equiv\frac{x^2}{4}-a\ \ln x+\frac{1}{2}\arg\Gamma(1/2+ia), \tag{B10}$$

taking the limit $z\to\infty$ and identifying the asymptotic coefficients,

$$\lim_{z\to\infty}\psi_{\rm osc}=\frac{1}{T_{\rm osc}}\sqrt{\frac{2}{z}}\exp[-i\phi(z)]+\frac{R_{\rm osc}}{T_{\rm osc}}\sqrt{\frac{2}{z}}\exp[i\phi(z)]. \tag{B11}$$

Note that $\exp(-ikz)$ and $\exp(ikz)$ are left and right moving, respectively, while $\sqrt{2/|z|}\exp[-i\phi(z)]$ and $\sqrt{2/|z|}\exp[i\phi(z)]$ are inward and outward moving, respectively.

Finally, the reflection probability $\mathcal{R}_{\rm hyb}\equiv|R_{\rm hyb}|^2$ for the potential $V_{\rm hyb}$ is obtained by finding $\nu_{\rm hyb}=\nu_{\rm osc}$ and $\mu_{\rm hyb}=\mu_{\rm osc}$ that would satisfy

$$\lim_{z\to-\infty}\psi_{\rm hyb}=\sqrt{\frac{2}{|z|}}\exp[i\phi(z)], \tag{B12}$$

finding then $A_{\rm hyb}$ and $B_{\rm hyb}$ from the continuity of the wave function and its first derivative at $z=0$, taking the limit $z\to\infty$ and identifying the coefficients,

$$\lim_{z\to\infty}\psi_{\rm hyb}=\frac{1}{T_{\rm hyb}}\exp(-ikz)+\frac{R_{\rm hyb}}{T_{\rm hyb}}\exp(ikz). \tag{B13}$$

These straightforward derivations give the reflection probabilities of Eqs. (27)–(29).

[1] R.J. Cook and R.K. Hill, Opt. Commun. **43**, 258 (1982).

[2] V.I. Balykin, V.S. Letokhov, Yu.B. Ovchinnikov, and A.I. Sidorov, Pis'ma Zh. Éksp. Teor. Fiz. **45**, 282 (1987) [JETP Lett. **45**, 353 (1987)]; Phys. Rev. Lett. **60**, 2137 (1988).

[3] M.A. Kasevich, D.S. Weiss, and S. Chu, Opt. Lett. **15**, 667 (1990).

[4] C.G. Aminoff, A.M. Steane, P. Bouyer, P. Desbiolles, J. Dalibard, and C. Cohen-Tannoudji, Phys. Rev. Lett. **71**, 3083 (1993).

[5] C.S. Adams, M. Sigel, and J. Mlynek, Phys. Rep. **240**, 143 (1994).

[6] M.G. Raizen, C. Salomon, and Q. Niu, Phys. Today **50** (7), 30 (1997); S.R. Wilkinson, C.F. Bharucha, K.W. Madison, Q. Niu, and M.G. Raizen, Phys. Rev. Lett. **76**, 4512 (1996); M. Ben Dahan, E. Peik, J. Reichel, Y. Castin, and C. Salomon, *ibid.* **76**, 4508 (1996).

[7] P. Szriftgiser, D. Guery-Odelin, M. Arndt, and J. Dalibard, Phys. Rev. Lett. **77**, 4 (1996).

[8] A. Aspect, R. Kaiser, N. Vansteenkiste, P. Vignolo, and C.I. Westbrook, Phys. Rev. A **52**, 4704 (1995).

[9] M. Arndt, P. Szriftgiser, and J. Dalibard, Phys. Rev. A **53**, 3369 (1996).

[10] Yu. B. Ovchinnikov, I. Manek, and R. Grimm, Phys. Rev. Lett. **79**, 2225 (1997).

[11] H. Ito, K. Sakaki, W. Jhe, and M. Ohtsu, Phys. Rev. A **56**, 712 (1997).

[12] T. Matsudo, H. Hori, T. Inoue, and T. Sakurai, Phys. Rev. A **55**, 2406 (1997).

[13] M.J. Renn, E.A. Donley, E.A. Cornell, C.E. Wieman, and D.Z. Anderson, Phys. Rev. A **53**, R648 (1996).

[14] C. Henkel, J.-Y. Courtois, R. Kaiser, C. Westbrook, and A.

Aspect, Laser Phys. **4**, 1042 (1994).
[15] A. Landragin, J.-Y. Courtois, G. Labeyrie, N. Vansteenkiste, C.I. Westbrook, and A. Aspect, Phys. Rev. Lett. **77**, 1464 (1996).
[16] P. Desbiolles, M. Arndt, P. Szriftgiser, and J. Dalibard, Phys. Rev. A **54**, 4292 (1996).
[17] B. Segev, R. Côté, and M.G. Raizen, Phys. Rev. A **56**, R3350 (1997).
[18] P. Kharchenko, J.F. Babb, and A. Dalgarno (private communication).
[19] L. Deng, E. Hagley, M. Kozuma, R. Lutwak, Yu. Ovchinnikov, J. Wen, K. Helmerson, W.D. Phillips, and S.L. Rolston (unpublished).
[20] V. Sandoghdar, C.I. Sukenik, E.A. Hinds, and S. Haroche, Phys. Rev. Lett. **68**, 3432 (1992); C.I. Sukenik, M.G. Boshier, D. Cho, V. Sandoghdar, and E.A. Hinds, *ibid.* **70**, 560 (1993).
[21] C. Cohen-Tannoudji, J. Dupont-Roc, and G. Grynberg, *Atom-Photon Interactions* (Wiley, New York, 1992).
[22] L.E. Lennard-Jones, Trans. Faraday Soc. **28**, 333 (1932).
[23] H.B.G. Casimir and D. Polder, Phys. Rev. **73**, 360 (1948).
[24] I.E. Dzyaloshinskii, E.M. Lifshitz, and L.P. Pitaevskii, Adv. Phys. **10**, 165 (1961).
[25] M. Marinescu, A. Dalgarno, and J.F. Babb, Phys. Rev. A **55**, 1530 (1997); P. Kharchenko, J.F. Babb, and A. Dalgarno, *ibid.* **55**, 3566 (1997).
[26] $n = 1.805$ is the index of refraction of Schott glass SFLG at 589 nm.
[27] R. Côté, H. Friedrich, and J. Trost, Phys. Rev. A **56**, 1781 (1997).
[28] N.T. Maitra and E.J. Heller, Phys. Rev. Lett. **78**, 3035 (1997).
[29] A. Landragin, G. Labeyrie, C. Henkel, R. Kaiser, N. Vansteenkiste, C.I. Westbrook, and A. Aspect, Opt. Lett. **21**, 1591 (1996); C. Henkel, K. Mølmer, R. Kaiser, N. Vansteenkiste, C.I. Westbrook, and A. Aspect, Phys. Rev. A **55**, 1160 (1997).
[30] A. Bambini and E. J. Robinson, Phys. Rev. A **45**, 4661 (1992).
[31] W. Zhang and D.F. Walls, Phys. Rev. Lett. **68**, 3287 (1992).
[32] H. Nha, and W. Jhe, Phys. Rev. A **56**, 729 (1997).
[33] C. Henkel, K. Mølmer, R. Kaiser, and C.I. Westbrook, Phys. Rev. A **56**, R9 (1997).
[34] H. Friedrich, *Theoretical Atomic Physics* (Springer-Verlag, New York, 1990).
[35] S. Flügge, *Practical Quantum Mechanics* (Springer-Verlag, New York, 1971).
[36] J. C. P. Miller, in *Handbook of Mathematical Functions*, edited by M. Abramowitz and I.A. Stegun (Dover, New York, 1972), Chap. 19.16.